MEDICAL ROBOTS

Magnetic soft microfiberbots for robotic embolization

Xurui Liu[1,2]†, Liu Wang[3,4]†, Yuanzhuo Xiang[2]†, Fan Liao[1,2], Na Li[1,2], Jiyu Li[3], Jiaxin Wang[5], Qingyang Wu[1,2], Cheng Zhou[1,2], Youzhou Yang[1,2], Yuanshi Kou[1,2], Yueying Yang[1,2], Hanchuan Tang[1,2], Ning Zhou[6], Chidan Wan[7], Zhouping Yin[8,9], Guang-Zhong Yang[10]*, Guangming Tao[2,11,12,13]*, Jianfeng Zang[1,2,9]*

Cerebral aneurysms and brain tumors are leading life-threatening diseases worldwide. By deliberately occluding the target lesion to reduce the blood supply, embolization has been widely used clinically to treat cerebral aneurysms and brain tumors. Conventional embolization is usually performed by threading a catheter through blood vessels to the target lesion, which is often limited by the poor steerability of the catheter in complex neurovascular networks, especially in submillimeter regions. Here, we propose magnetic soft microfiberbots with high steerability, reliable maneuverability, and multimodal shape reconfigurability to perform robotic embolization in submillimeter regions via a remote, untethered, and magnetically controllable manner. Magnetic soft microfiberbots were fabricated by thermal drawing magnetic soft composite into microfibers, followed by magnetizing and molding procedures to endow a helical magnetic polarity. By controlling magnetic fields, magnetic soft microfiberbots exhibit reversible elongated/aggregated shape morphing and helical propulsion in flow conditions, allowing for controllable navigation through complex vasculature and robotic embolization in submillimeter regions. We performed in vitro embolization of aneurysm and tumor in neurovascular phantoms and in vivo embolization of a rabbit femoral artery model under real-time fluoroscopy. These studies demonstrate the potential clinical value of our work, paving the way for a robotic embolization scheme in robotic settings.

INTRODUCTION

Cerebral aneurysms and brain tumors are leading causes of mortality, killing more than 750,000 people annually worldwide (*1*, *2*). Before an open surgery is administered, embolization recently has become a prevailing minimally invasive treatment for cerebral aneurysms and brain tumors (*3*, *4*). In a typical embolization, a surgeon inserts a slender guidewire or catheter into the femoral artery of the patient and manually pushes or twists it to the target lesion in the brain through the blood vessels, followed by the delivery of embolic agents to block the target lesion (*5*–*7*). For example, a surgeon can deliver metallic coils through the catheter to seal off the cerebral aneurysm, which stabilizes the aneurysm and minimizes the risk of rupture. Particulates are another common embolic agent in tumor embolization. As the catheter is pushed into the vessels feeding a tumor, particles are delivered to cut off the blood supply, starving the tumor for accelerated removal (*8*–*15*). However, current embolization by pushing or twisting a passive guidewire/catheter with a preshaped tip is often limited by its low steerability through complex vascular networks, because the guidewire/catheter has difficulty turning at bifurcation branches of blood vessels. As a result, embolic agents may not be accurately delivered to the target lesion, leading to safety complications such as blockage of normal vessels. In addition, the surgeon suffers from the accumulated radiation when manually pushing or twisting the guidewire/catheter under the x-ray imaging system. Therefore, there has been a high demand for a next-generation embolization technique with high steerability for targeted delivery of embolic agents and a remotely controllable operation for a radiation-free workplace.

Recently, active robots that can be remotely steered in the blood vessel have shown great promise in robotic embolization (*16*–*27*). One widely used strategy is designing guidewire/catheter robots with an active tip that can bend in response to external stimuli, such as hydraulic pressure (*19*), electricity (*20*), and magnetic fields (*21*–*25*). For example, Kim *et al.* (*22*) have developed a guidewire robot with a ferromagnetic tip that can bend by remotely applying magnetic fields. Such an active guidewire robot has shown enhanced steerability in blood vessels and the ability to deliver embolic agents to an aneurysm (*23*). However, maneuvering guidewires/catheters (regardless of passive and active tips) intrinsically requires tethered operation, which is of great difficulty when the slender guidewires/catheters are highly distorted, buckled, and looped in confined and tortuous blood vessels. This difficulty gets even more pronounced when the target lesion is located in the submillimeter regions. To address this issue, another strategy is to develop small-scale untethered robots that can navigate

[1]School of Integrated Circuits, Huazhong University of Science and Technology, Wuhan 430074, China. [2]Wuhan National Laboratory for Optoelectronics, Huazhong University of Science and Technology, Wuhan 430074, China. [3]CAS Key Laboratory of Mechanical Behavior and Design of Materials, Department of Modern Mechanics, University of Science and Technology of China, Hefei 230026, PR China. [4]State Key Laboratory of Nonlinear Mechanics, Institute of Mechanics, Chinese Academy of Science, 15 Beisihuan West Road, Beijing 100190, China. [5]Department of Urology, Tongji Hospital, Tongji Medical College, Huazhong University of Science and Technology, Wuhan 430030, PR China. [6]Division of Cardiology, Department of Internal Medicine, Tongji Hospital of Tongji Medical College of Huazhong University of Science and Technology, Wuhan 430074, China. [7]Department of Hepatobiliary Surgery, Union Hospital, Tongji Medical College, Huazhong University of Science and Technology, Wuhan 430074, China. [8]Flexible Electronics Research Center, State Key Laboratory of Digital Manufacturing Equipment and Technology, School of Mechanical Science and Engineering, Huazhong University of Science and Technology, Wuhan, Hubei 430074, China. [9]State Key Laboratory of Intelligent Manufacturing Equipment and Technology, School of Mechanical Science and Engineering, Huazhong University of Science and Technology, Wuhan 430074, China. [10]Institute of Medical Robotics, Shanghai Jiao Tong University, Shanghai 200240, China. [11]State Key Laboratory of Material Processing and Die & Mould Technology, School of Materials Science and Engineering, Huazhong University of Science and Technology, Wuhan 430074, China. [12]Key Laboratory of Vascular Aging, Ministry of Education, Tongji Hospital, Tongji Medical College, Huazhong University of Science and Technology, Wuhan 430030, China. [13]Institute of Medical Equipment Science and Engineering, Huazhong University of Science and Technology, Wuhan 430074, China.
*Corresponding author. Email: gzyang@sjtu.edu.cn (G.-Z.Y.); tao@hust.edu.cn (G.T.); jfzang@hust.edu.cn (J.Z.)
†These authors contributed equally to this work.

blood vessels as a substitute for guidewires/catheters. For example, flow-driven magnetic swarm (*28*), magnetic particles (*29*), and magnetic anchors (*30*) have been reported for potential application of tumor embolization in submillimeter regions. However, because they are passively carried by blood flow, these untethered robots lack reliable maneuverability for navigation in flow conditions, which may lead to severe complications of nontargeted embolization (*7*, *31*). Although many other untethered robots (for example, sheet-shaped magnetic robots and magnetic stents) have shown improved navigation capability (for example, adaptive locomotion) in flow conditions (*32*, *33*), they have not been demonstrated for robotic embolization because of limited shape-morphing ability at the target lesion. Therefore, it remains a challenge for active robots to demonstrate high steerability in tortuous blood vessels (especially in submillimeter regions), reliable maneuverability in flow conditions, and shape-morphing capability at target lesions (see table S1).

Here, we present magnetic soft microfiber robots (hereafter referred to as microfiberbots) with enhanced steerability, reliable maneuverability, and shape reconfigurability to perform robotic embolization in a remotely controllable manner (Fig. 1A and movie S1). Magnetic soft microfiberbots have a helical geometry with a customizable diameter (Fig. 1B) that can be compatible with existing catheters to maximize their clinical effectiveness. A standard catheterization can be first performed by threading a commercial catheter through blood vessels until the intravascular advancement is stopped. Thereafter, the microfiberbots can be deployed into blood vessels through the catheter. Enabled by the contact friction, the microfiberbot can anchor to the blood vessel after deployment without being flushed away by blood flow. By remotely applying magnetic fields, the microfiberbot can be actively steered in the blood flow (both upstream and downstream) via helical propulsion. The microfiberbots can be elongated for passing narrow regions and aggregated at the target lesion. The aggregated microfiberbot can either block the blood flow to the target aneurysm/tumor or protect the normal blood vessel, allowing for three embolization applications: aneurysm coil embolization, tumor coil embolization, and tumor particle embolization (Fig. 1A). We demonstrate both in vitro embolization of aneurysm and tumor in neurovascular phantoms and in vivo embolization of a rabbit femoral artery model under real-time fluoroscopy. As a supplement to conventional catheter-based embolization, our work presents a substantial advancement for the minimally invasive treatment of cerebral aneurysms and brain tumors in a robotic setting.

RESULTS

Shape-morphing capability

The magnetic composite was first prepared by uniformly dispersing neodymium-iron-boron (NdFeB) microparticles in a thermoplastic matrix [poly(styrene-*b*-(ethylene-*co*-butylene)-*b*-styrene) (SEBS)]. The volume fraction of NdFeB is 20%. Using a thermal drawing technique (Fig. 1B and fig. S1), straight magnetic microfibers with

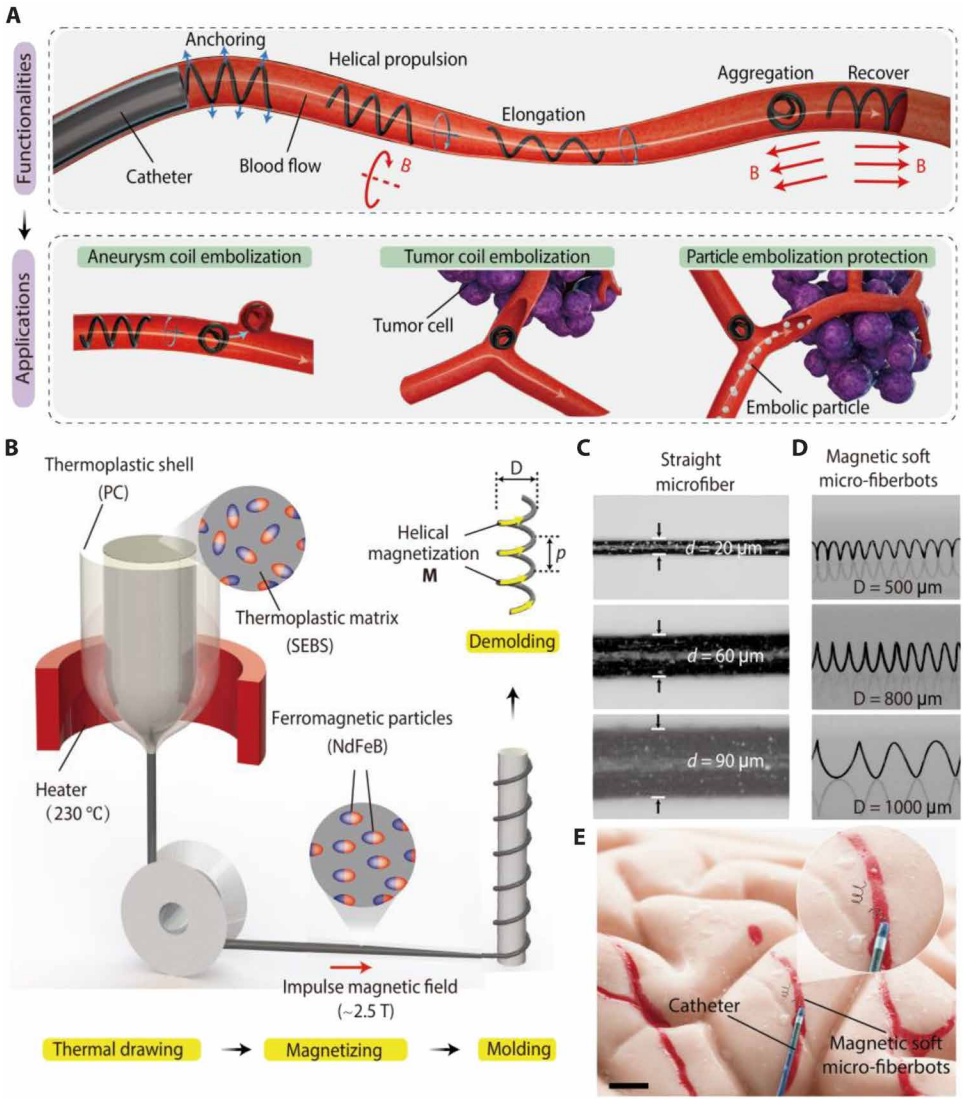

Fig. 1. Magnetic soft microfiberbots for robotic embolization. (**A**) Schematic illustration of functionalities and potential applications of magnetic soft microfiberbots. The microfiberbot can anchor to a blood vessel after being released, navigate in the blood vessels via helical propulsion, pass through narrow regions by elongation, and block the blood flow by aggregation. The aggregated microfiberbots can be used as embolic agents for coil embolization of aneurysms and tumors and as protection devices for selective particle embolization of tumors. (**B**) Fabrication process of magnetic soft microfiberbots: thermal drawing of magnetic soft microfiber, magnetizing by a strong impulse magnetic field (2.5 T), and molding/demolding into a helix shape. (**C**) Optical imaging of magnetic soft microfibers with different fiber diameters denoted as *d*. (**D**) Optical images of magnetic soft microfiberbots with different helical diameters denoted as *D*. (**E**) An image of magnetic soft microfiberbots deployed via a Terumo 2.6-Fr catheter to the surface of the brain phantom. Scale bar, 5 mm.

various diameters d (Fig. 1C) were fabricated. By applying an impulse magnetic field (2.5 T), the straight magnetic microfiber can be fully magnetized along the fiber direction. Thereafter, by coiling around a cylindrical mold and demolding after curing, the straight micro fiber can be transformed into a magnetic soft microfiberbot with a helical magnetization **M** along its body. By changing the geometry of the cylindrical mold, the helical pitch p (Fig. 1B) and helical diameter D (Fig. 1D) of microfiberbots can be readily tuned. A representative microfiberbot with $d = 60$ μm, $p = 800$ μm, and $D = 800$ μm was selected for demonstrating embolization in submillimeter regions in this work (Fig. 1E).

When the microfiberbot reached a vessel segment that has an inner diameter (denoted as H) slightly smaller than that of the microfiberbot, it anchored to the blood vessel because of the contact friction without being flushed away by the blood flow (Fig. 2A). Finite element simulation validates that the total contact friction is larger than the fluidic drag force (fig. S2). Despite the sufficient friction force, the maximum contact pressure with the vessel wall is as low as 4.3 kPa, which is much smaller than the threshold pressure for rupturing the blood vessel [12 kPa (*34*, *35*)]. The helical magnetization profile **M** endows the microfiberbot with a net magnetization $\mathbf{M}_{net}$ (Fig. 2A) along its central axis. By applying an actuation magnetic field **B** that has the same direction as $\mathbf{M}_{net}$, the microfiberbot is elongated. The helical diameter gradually reduces as the magnetic field strength increases (fig. S3). Conversely, when **B** is opposite to $\mathbf{M}_{net}$, the microfiberbot is aggregated (Fig. 2A and movie S2) and its length gradually reduces as the magnetic field strength increases (fig. S3). Such aggregation/elongation shape morphing is fully reversible even after 1000 cycles as validated by three microfiberbots with different pitches (fig. S4). Moreover, the microfiberbot can still recover its helical shape even after a compression test under a rigid punch, manifesting high elasticity and robustness (fig. S5).

Magnetic maneuverability in flow conditions

Figure 2B illustrates the strategy for magnetically maneuvering the microfiberbot in flow conditions. A cubic magnet (5 cm by 5 cm by 5 cm, residual magnetic flux density $\mathbf{B_r} = 1.38$ T) was adopted as an actuation source (figs. S6 and S7). The magnet was manipulated by a six–degree of freedom (DOF) robotic arm that can precisely control its current position denoted as (x, y) in the xyz coordinate system

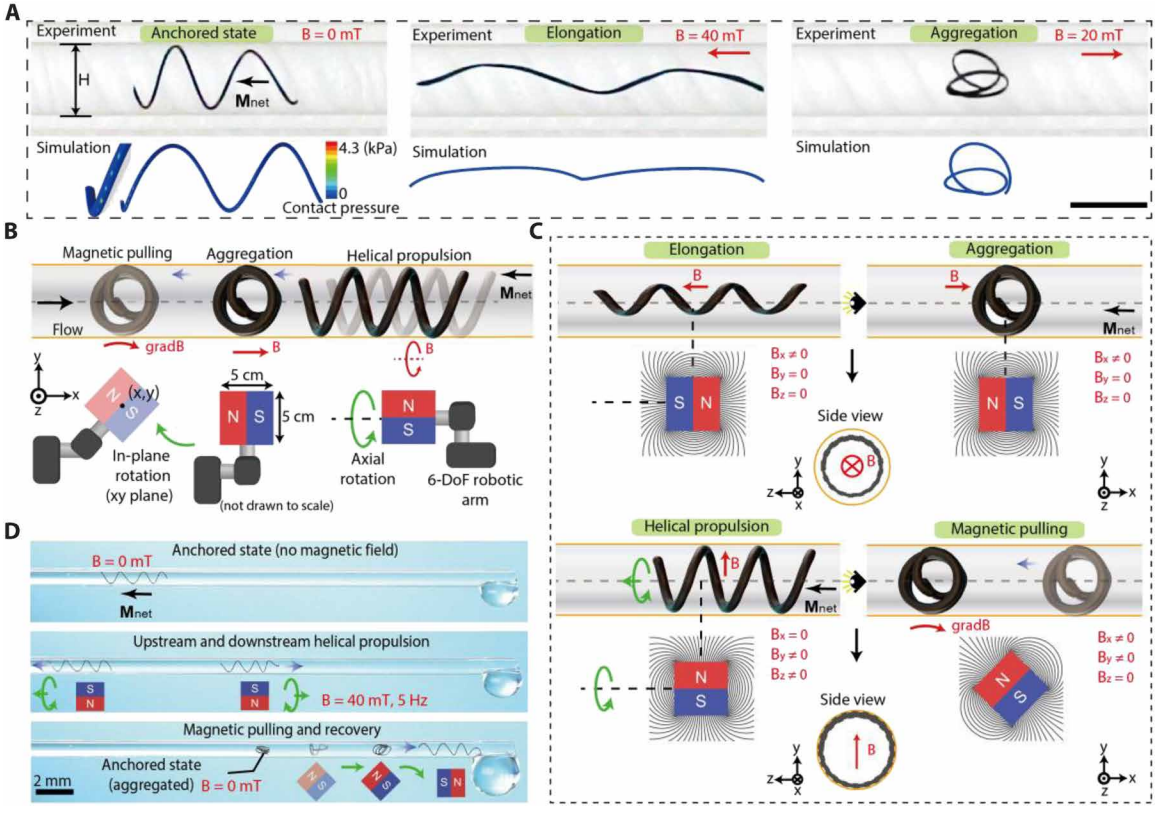

Fig. 2. Shape-morphing capability and magnetic maneuverability in flow conditions. (**A**) The microfiberbot can anchor to the vessel in the absence of magnetic fields. By further applying static magnetic field **B** parallel to its net magnetization (denoted as $\mathbf{M}_{net}$), the magnetic soft microfiberbot can have reversible elongated and aggregated states. Scale bar, 1 mm. The finite element analysis (FEA) reveals that the maximum contact pressure occurring between the microfiberbots and the vessel wall is 4.3 kPa. (**B**) Schematic illustration of manipulating the microfiberbot by controlling a cubic magnet with a 6-DOF robotic arm. The helical propulsion is enabled by axially rotating the magnet (rotating axis is parallel with the x axis), whereas magnetic pulling is enabled by rotating the magnet in the xy plane. (**C**) The magnetic soft microfiberbots can perform aggregation and elongation shape morphing by changing the external magnetic field. The elongated state of the microfiberbot is achieved by controlling the magnet to generate the magnetic field along with $\mathbf{M}_{net}$, and the aggregated state is achieved by controlling the magnet to generate the magnetic field opposite $\mathbf{M}_{net}$. The upstream helical propulsion is achieved by rotating the magnet in a clockwise manner, and magnetic pulling is achieved by moving the magnet. (**D**) Experimental pictures show that the microfiberbot ($d = 60$ μm, $p = 800$ μm, and $D = 800$ μm) can steadily anchor to a vessel phantom (inner diameter $H = 800$ μm) in the absence of magnetic fields, achieve upstream/downstream helical propulsion under rotating magnetic fields (**B** = 40 mT, frequency of 5 Hz), undergo magnetic pulling under a magnetic field gradient, and recover to the helical shape. Scale bars, 2 mm.

via axial rotation (rotating axis parallel with x axis) and in-plane rotation (in the xy plane) (fig. S8). The rotating magnetic fields allow for high flexibility for manipulating the untethered magnetic soft microfiberbot (*36*). By axially rotating while moving the magnet leftward, we can maneuver the microfiberbot to the left via helical propulsion. Aside from high flexibility of control, such a helical propulsion motion is different from direct pulling by magnetic body force

$$\mathbf{f} = (\mathrm{grad}\mathbf{B})\mathbf{M} \tag{1}$$

where $\mathbf{M}$ and $\mathbf{B}$ are the magnitudes of the magnetization and the applied magnetic field, respectively, for which a large magnetic field gradient

$$\mathrm{grad}\mathbf{B} = \left[\frac{\partial \mathbf{B}}{\partial x}, \frac{\partial \mathbf{B}}{\partial y}, \frac{\partial \mathbf{B}}{\partial z}\right]^{\mathrm{T}} \tag{2}$$

is required (*37*–*39*). When the microfiberbot reaches the target lesion, by rotation of 90° in the xy plane, we can generate a local actuation magnetic field $\mathbf{B}$ opposite to $\mathbf{M}_{\mathrm{net}}$, leading to the aggregation shape morphing. If further magnetic pulling operation is needed, we can further rotate the magnet in the xy plane by 45° to generate a field gradient gradB as shown in fig. S7. Therefore, the body force $\mathbf{f}$ will pull the microfiberbot to move with the magnet (*37*). This magnetic pulling maneuvering will finally allow us to pull the aggregated microfiberbot to fill the aneurysm for embolization application. Corresponding actuation magnetic fields shown by ($\mathbf{B}_x$, $\mathbf{B}_y$, $\mathbf{B}_z$) in each maneuvering process are depicted in Fig. 2C. Because the size of the microfiberbot is much smaller than that of the cubic magnet and the actuation distance, the actuating magnetic field can be treated as uniform (fig. S6B) when the microfiberbot is actuated by magnetic fields on the middle plane of $x = 0$ or $y = 0$. Therefore, when the microfiberbot is either elongated or aggregated, the dominant magnetic field component is $\mathbf{B}_x$, with $\mathbf{B}_y$ and $\mathbf{B}_z$ equaling zero. When the microfiberbot undergoes helical propulsion, the magnetic field component $\mathbf{B}_x$ becomes zero. As the magnet rotates, nonzero components appear in the x, y, and z directions of the magnetic fields surrounding the microfiberbot, generating a magnetic body force that pulls the microfiberbot. Details of the magnetic maneuvering processes executed by the robotic arm equipped with a permanent magnet are illustrated in movie S3.

To validate the shape morphing and magnetic maneuvering of the microfiberbot in flow conditions, we prepared a vessel phantom with an inner diameter H = 800 μm and filled it with simulated blood (50% glycerol solution; viscosity at around 4 mPa·s). The flow rate was set as 100 mm/s via a pump system to mimic the typical blood flow in submillimeter regions of neurovascular networks (*40*). We first showed that the microfiberbot can stably anchor to the vessel in the absence of magnetic fields (Fig. 2D). By tuning the strength and the frequency of the rotating magnetic field, the helical propulsion velocity can be adjusted (fig. S3C). If the simulated blood is not flowing, the helical propulsion velocity of the microfiberbot can reach up to 1.6 mm/s under a rotating magnetic field $\mathbf{B}$ = 40 mT at a frequency of 5 Hz. When the flow rate is 100 mm/s, the upstream and downstream helical propulsion velocities of the microfiberbot change to 0.32 and 1.75 mm/s, respectively. It is also worth noting that the aggregated microfiberbot can also anchor to the blood vessel when the magnetic field is removed because of friction. This anchoring capability at the aggregated state allows the microfiberbot to be further pulled by applying a magnetic field gradient grad$\mathbf{B}$ that generates magnetic body force $\mathbf{f}$. For example, by tuning the magnet's orientation of 45° in the xy plane, the aggregated microfiberbot can be further pulled inside the vessel (Fig. 2D). The helical shape of the microfiberbot is recovered when aligning the magnetic field $\mathbf{B}$ with a net magnetization $\mathbf{M}_{\mathrm{net}}$. It is also worth noting that such shape-morphing and propulsion capabilities may not be seriously affected by the size of the microfiberbot. We showed that a microfiberbot with a 500-μm diameter still preserves comparable upstream propulsion velocity to that of the 800-μm microfiberbot in flow conditions up to a 200 mm/s flow rate (fig. S9 and movie S4).

Catheter-assisted deployment

Considering that there is a long way from the incision (usually at the femoral arteries) to the target lesion in the brain, our microfiberbot can be combined with existing medical catheters to reduce the operation time while increasing embolization safety. Here, a representative medical catheter [MicroVention Terumo, tip inner diameter = 0.027 inch (685 μm), distal outer diameter = 0.034 inch (866 μm); Fig. 1E] was selected to demonstrate the catheter-assisted deployment (Fig. 3). We showed that the microfiberbot (D = 800 μm) can be easily injected into the catheter via a 200-μm needle syringe (Fig. 3A). Because of the elastic nature and high robustness, the highly coiled microfiberbot can quickly recover its helical shape after injection (less than 1 s). When traveling inside the catheter, the microfiberbot can be readily tracked by x-ray imaging (Fig. 3B). Although the catheter cannot directly reach the target lesion, it still paves a safe way for the microfiberbot to approach the target lesion as closely as possible. Thereafter, the microfiberbot is remotely maneuvered by magnetic fields to complete the rest of the journey to the target lesion.

A blood vessel phantom with bifurcation branches (fabricated using a sacrificial template method; fig. S10) was selected as an example (Fig. 3, C and D). The mechanical properties (Young's modulus is around 2 MPa) and contact friction coefficient (0.1) were carefully tuned to mimic those of human blood vessels. We assumed that the catheter can only reach the main blood vessel and two target lesions located on the bifurcation branches. To reach target 1, the microfiberbot can be released at the first bifurcation in the main vessel. Thereafter, the microfiberbot can be magnetically maneuvered to target 1 by helical propulsion, followed by on-demand aggregation. Similarly, to reach target 2, the catheter can be first threaded to the second bifurcation, and then the microfiberbot can be released, magnetically steered, and aggregated at target 2. Detailed catheter-assisted deployment is shown in movie S5. By combining with existing medical catheters, the clinical effectiveness of the microfiberbot can be maximized by reducing magnetic maneuvering, especially when multiple microfiberbots need to be deployed. In comparison, we show that without the microfiberbot, the catheter can only reach the second bifurcation. If coils are directly delivered at the second bifurcation, targeted embolization cannot be ensured (fig. S11).

High steerability in submillimeter regions

The steerability of soft robots in blood vessels is often characterized by the angle of bifurcation branches and the diameter of the accessible blood vessel (see table S1). To demonstrate the high steerability in submillimeter regions, we fabricated two phantoms of blood vessels (Fig. 4) with uniform diameter D = 800 μm. The first phantom had two bifurcation branches with angles of 30° and 60° (Fig. 4A), respectively, and the second phantom had two bifurcation branches with angles of 90° and 120° (Fig. 4B), respectively. We showed that the microfiberbot can easily turn to the bifurcation branches of 30° via

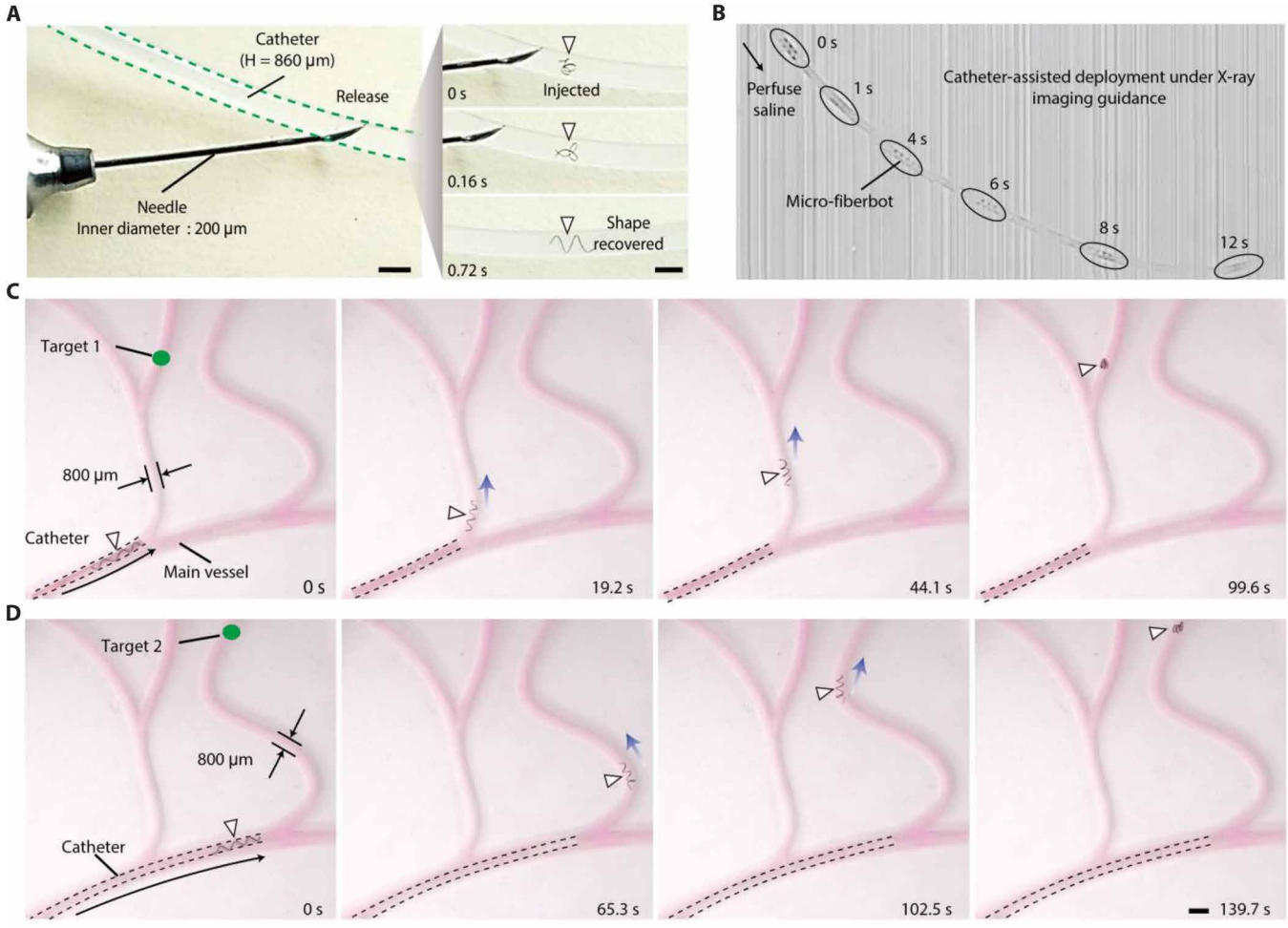

Fig. 3. Catheter-assisted deployment of the microfiberbot. (**A**) The microfiberbot can be injected into a commercial catheter with a microneedle syringe. The microfiberbot quickly recovers its helical shape after injection. (**B**) The microfiberbot travels inside the catheter by perfusing saline under x-ray imaging guidance. Catheter-assisted deployment of the microfiberbot for embolization at (**C**) target 1 and (**D**) target 2 in a blood vessel phantom with bifurcation branches. All scale bars, 1 mm.

downstream helical propulsion. By reversely rotating the magnet, the microfiberbot can return via upstream helical propulsion. This reverse maneuvering implied that, if the microfiberbot goes into a wrong branch vessel, it can be readily reoriented to the right track. After that, the microfiberbot can be further maneuvered to a 60° bifurcation branch vessel. In the second phantom, because the bifurcation angles are large, the microfiberbot needs to first turn its "head" into the branch vessel under a rotating magnetic field. Thereafter, a magnetic field **B** parallel to $\mathbf{M}_{net}$ is applied to stretch the microfiberbot, dragging it into the branch vessel. Once the whole body is steered to the bifurcation branches, the stretched microfiberbot quickly recovers its helical shape, continuing the helical propulsion in the branch vessel (movie S6). In addition to the high steerability in large-angle bifurcation vessels, we further demonstrated that the microfiberbot can simply pass through a narrowing vessel with a minimum diameter of 100 μm in Fig. 4C and movie S7. The microfiberbot was stretched by applying a parallel magnetic field so that it can pass the narrowing vessel with the flow. Considering that real blood vessels are three dimensional (3D), we further presented the steerability of the microfiberbot in an S-shaped (movie S8) and 3D blood vessel phantom (movie S9) in Fig. 4, D and E, respectively. Both results showed that the microfiberbot can be quickly steered through the blood vessel phantom. In contrast, we demonstrated that the commercial catheter cannot be directed to the bifurcation and narrowing branches, as shown in fig. S12.

In vitro demonstration of robotic embolization

To demonstrate the potential for treating cerebral aneurysms and brain tumors, we first performed robotic embolization demonstrations in submillimeter neurovascular vessel phantoms, which include aneurysm coil embolization (Fig. 5, A and B), tumor coil embolization (Fig. 5, C and D), and tumor particle embolization protection (Fig. 5, E to H). The first blood vessel phantom (H = 800 μm) had a saccular aneurysm (Fig. 5A), and the second blood vessel phantom had three bifurcation branches with thinner diameters (H = 500 μm) that are labeled as branch 1, branch 2, and branch 3 (Fig. 5, C to H). In aneurysm coil embolization, the microfiberbot was first helically propelled to the aneurysm and then transformed into the aggregated state. Via magnetic pulling, the aggregated microfiberbot can be pulled to fill the aneurysm (Fig. 5A and movie S10). It is evident that the flow to the aneurysm was reduced after the aneurysm was filled (Fig. 5B). In tumor coil embolization, branch 2 was assumed to be the tumor vessel,

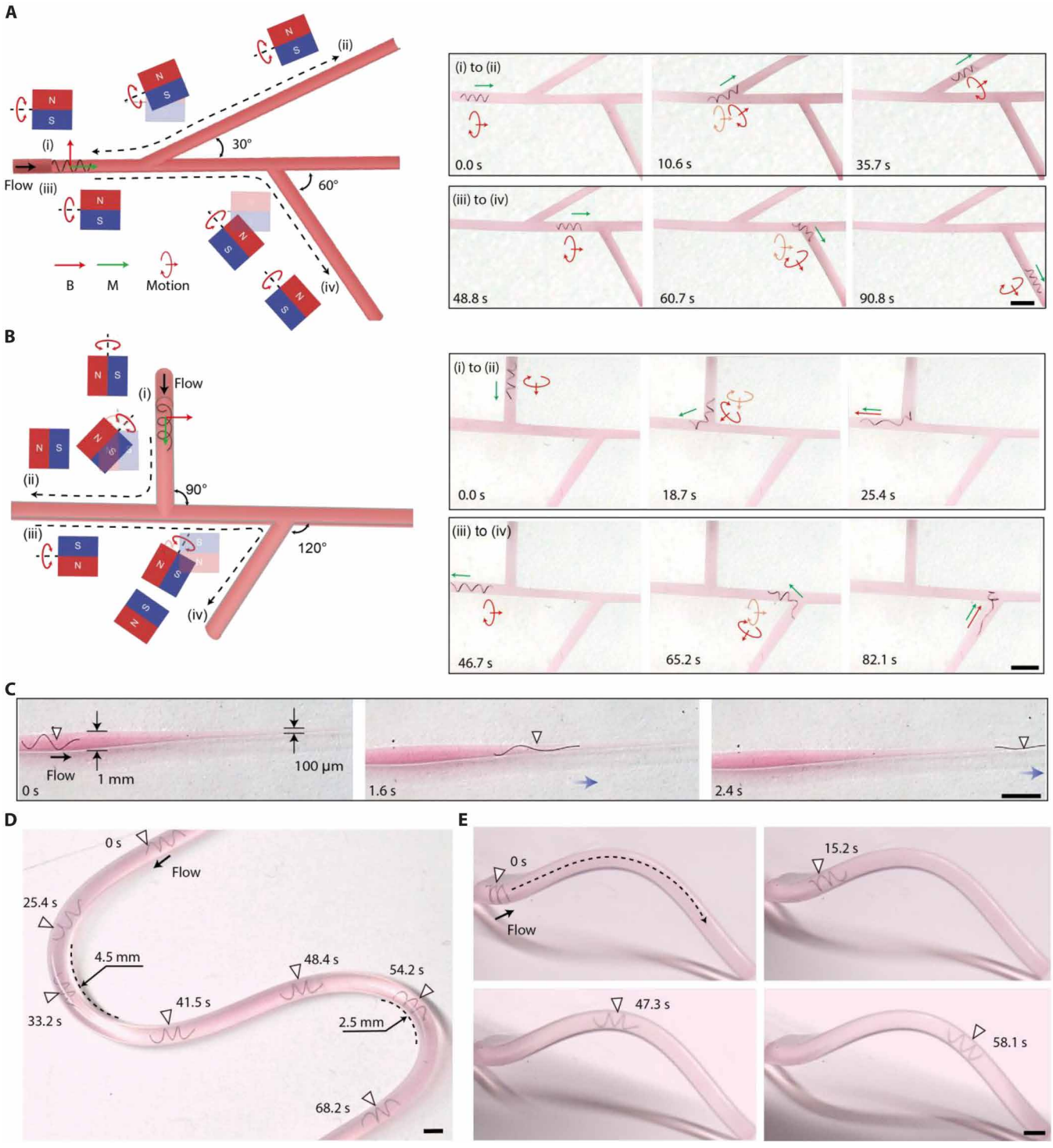

Fig. 4. Steerability of the microfiberbot in submillimeter regions. (**A**) Schematic illustration and experimental demonstration of the microfiberbot navigating in a blood vessel phantom with bifurcation branches of 30° and 60°. (**B**) Schematic illustration and experimental pictures of the microfiberbot navigating in a blood vessel phantom with bifurcation branches of 90° and 120°. Scale bars in (A) and (B), 2 mm. (**C**) Experimental demonstrations of the microfiberbot navigating in a vessel phantom with a narrowing diameter (1 mm to 100 µm). (**D**) Demonstration of the microfiberbot navigating an S-shaped vessel phantom. (**E**) Demonstrations of the microfiberbot navigating a 3D vessel phantom. Scale bars in (C) to (E), 1 mm.

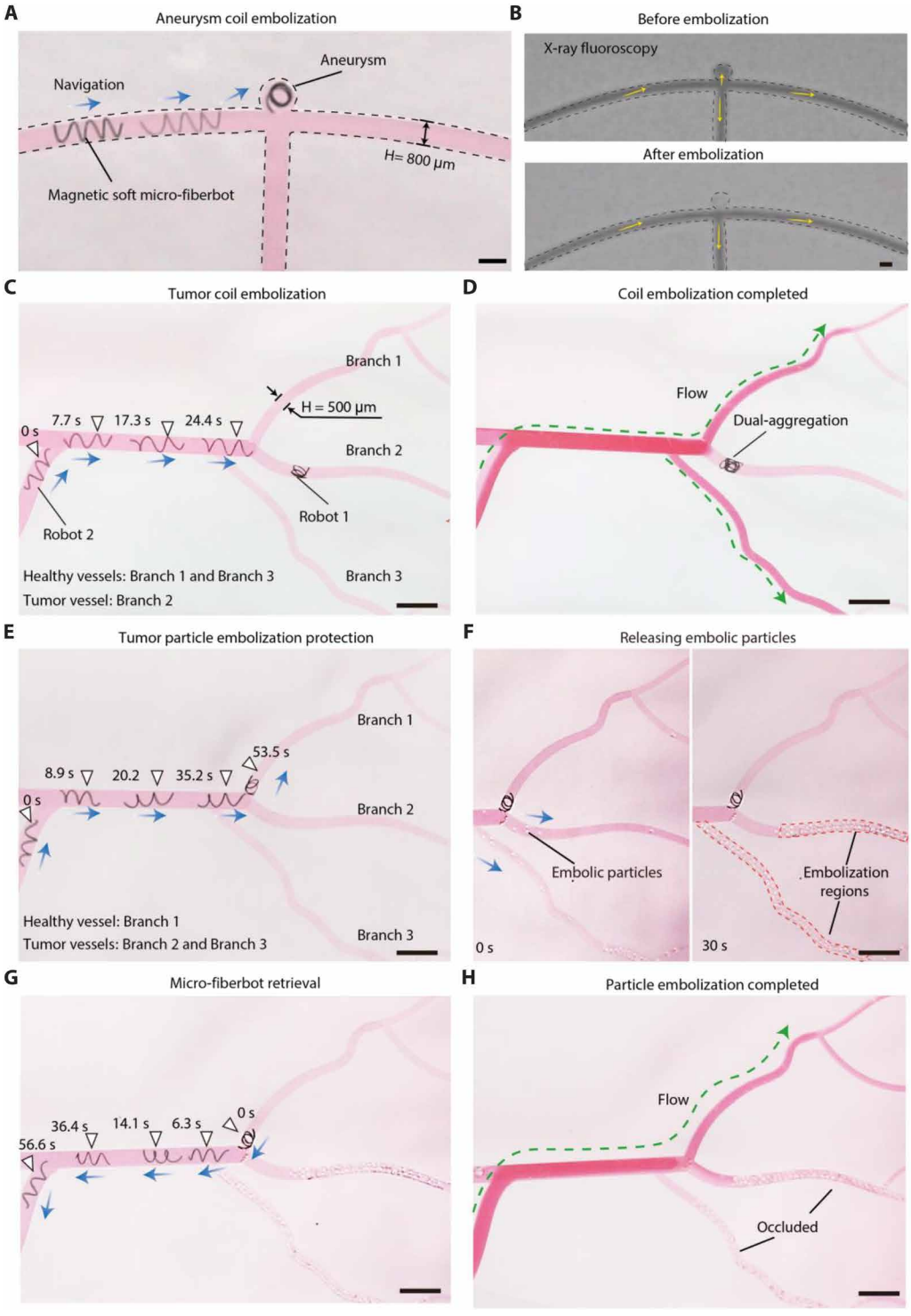

Fig. 5. In vitro robotic embolization in neurovascular vessel phantoms. (**A**) Demonstration of aneurysm coil embolization by magnetic soft microfiberbot. Scale bar, 1 mm. (**B**) Validation of the embolization results under x-ray fluoroscopy. The flow into the aneurysm is reduced after coil embolization. Scale bar, 1 mm. (**C**) Demonstration of tumor coil embolization in which branch 2 is assumed to be a tumor vessel. Two microfiberbots are steered subsequently to completely occlude branch 2. (**D**) The contrast agent is released to validate the occluded branch 2. (**E**) Demonstration of tumor particle embolization protection in which branch 1 is assumed to be a healthy vessel. (**F**) After the microfiberbot blocks the healthy branch 1, the embolic particles are released to occlude tumor vessels (branches 2 and 3). (**G**) The microfiberbot can be safely retrieved after particle embolization is completed. (**H**) The contrast agent is released to validate the occluded vessel branches 2 and 3. Scale bars in (C) to (H), 2 mm.

whereas branches 1 and 3 were the healthy blood vessels (Fig. 5C). A microfiberbot was first magnetically steered to branch 2 and aggregated. However, it was found that one aggregated microfiberbot alone cannot completely occlude branch 2 (movie S11). Therefore, a second microfiberbot was deployed for a dual aggregation in branch 2. Compared with one aggregated microfiberbot, two aggregated microfiberbots notably increased the blocking ratio (defined as the cross-sectional area of the microfiberbots divided by the blood vessel; Fig. 6A) that almost blocked flow in branch 2 after embolization (Fig. 5D). In tumor particle embolization protection, branches 2 and 3 were assumed to be tumor vessels, whereas branch 1 was the healthy vessel (Fig. 5E). To prevent the embolic particles from flowing into healthy branch 1, a microfiberbot was first magnetically steered to branch 1 and aggregated. Then, embolic particles (average diameter 250 μm) were released into the flow to selectively occlude branches 2 and 3 (Fig. 5F). After the particle embolization is completed, the aggregated microfiberbot can be recovered and safely retrieved (Fig. 5G and movie S12). It was confirmed that the tumor vessels (branches 2 and 3) were successfully occluded, whereas the healthy vessel (branch 1) was protected (Fig. 5H). Note that some particles may still be able to pass through the occluded area with one aggregated microfiberbot. To achieve a large blocking ratio, dual aggregation can be performed, and the block ratio can reach up to 88% (Fig. 6, A and B). Here, the dual aggregation is enabled by the independent actuation of each microfiberbot in sequence. As shown in Fig. 2C, the rotating magnetic field for helical propulsion is zero along the $\mathbf{M}_{net}$ direction ($\mathbf{B}_x = 0$ in the x direction), whereas elongation/aggregation requires $\mathbf{B}_x \neq 0$. Therefore, if a microfiberbot has already aggregated at the target lesion, the magnetic field guiding the helical propulsion of subsequent microfiberbots will not influence the aggregated one. This permits occlusions at multiple blood vessel branches (Fig. 6C) and even facilitates quadruple aggregation at the same target (Fig. 6D and movie S13).

In vivo demonstration of robotic embolization in a rabbit

We further demonstrated in vivo robotic embolization of a rabbit blood vessel on the right hind leg (diameter is from 500 to 800 μm) under real-time fluoroscopy (Fig. 7A). The microfiberbot was first injected into the femoral artery through a Terumo 2.6-French (Fr) catheter (Fig. 7B). The tortuous vessel was marked with four sites

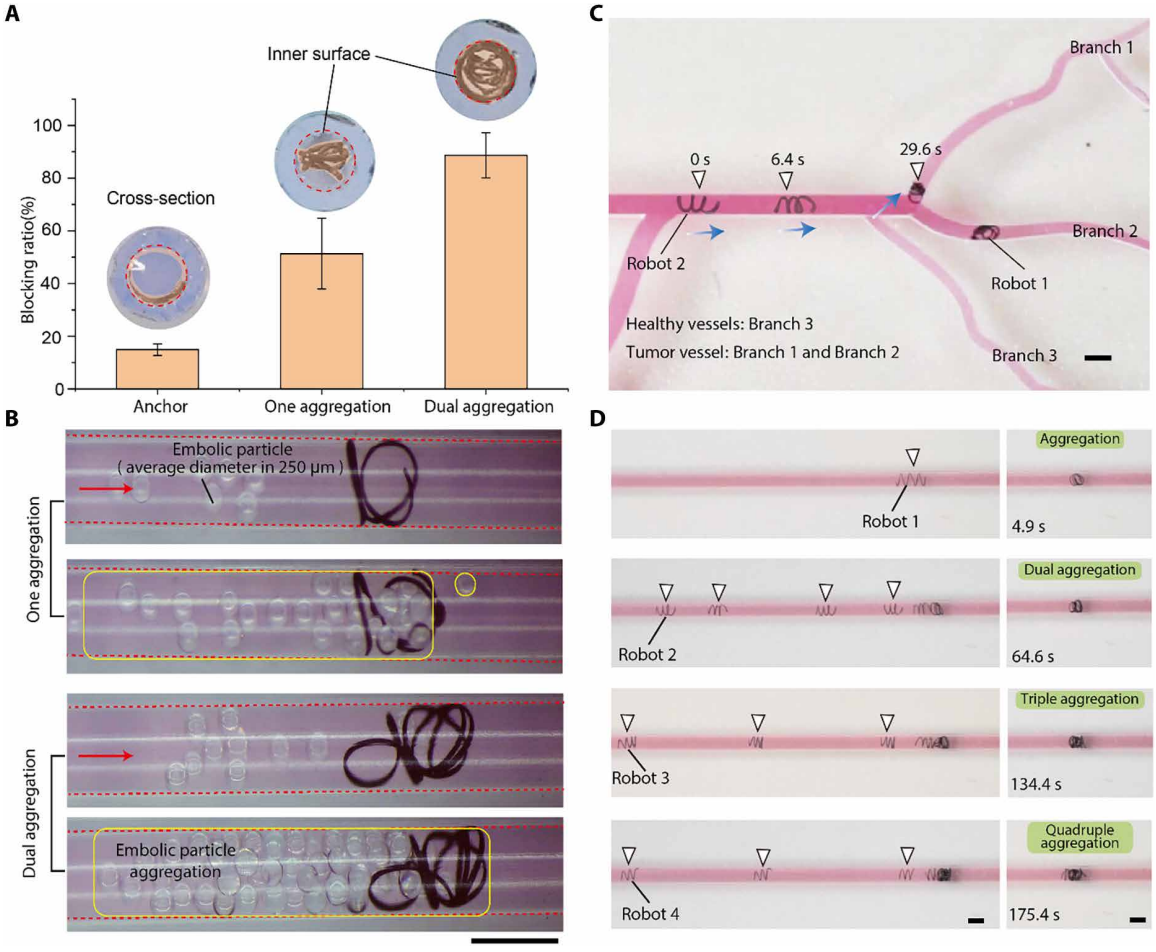

Fig. 6. Robotic embolization with multiple microfiberbots. (**A**) The blocking ratio is defined as the ratio of the cross-sectional area between the aggregated microfiberbots and the blood vessels. The average blocking ratios (± SD) are 14.92 ± 2.2%, 51.35 ± 13.4%, and 88.65 ± 8.6% for the respective measurements ($N = 3$). (**B**) Demonstration showing that particles are fully blocked with dual aggregated microfiberbots. (**C**) Demonstration of aggregated microfiberbot in different vessel branches. (**D**) Demonstration of quadruple aggregation at the same target in a vessel phantom. All scale bars, 1 mm.

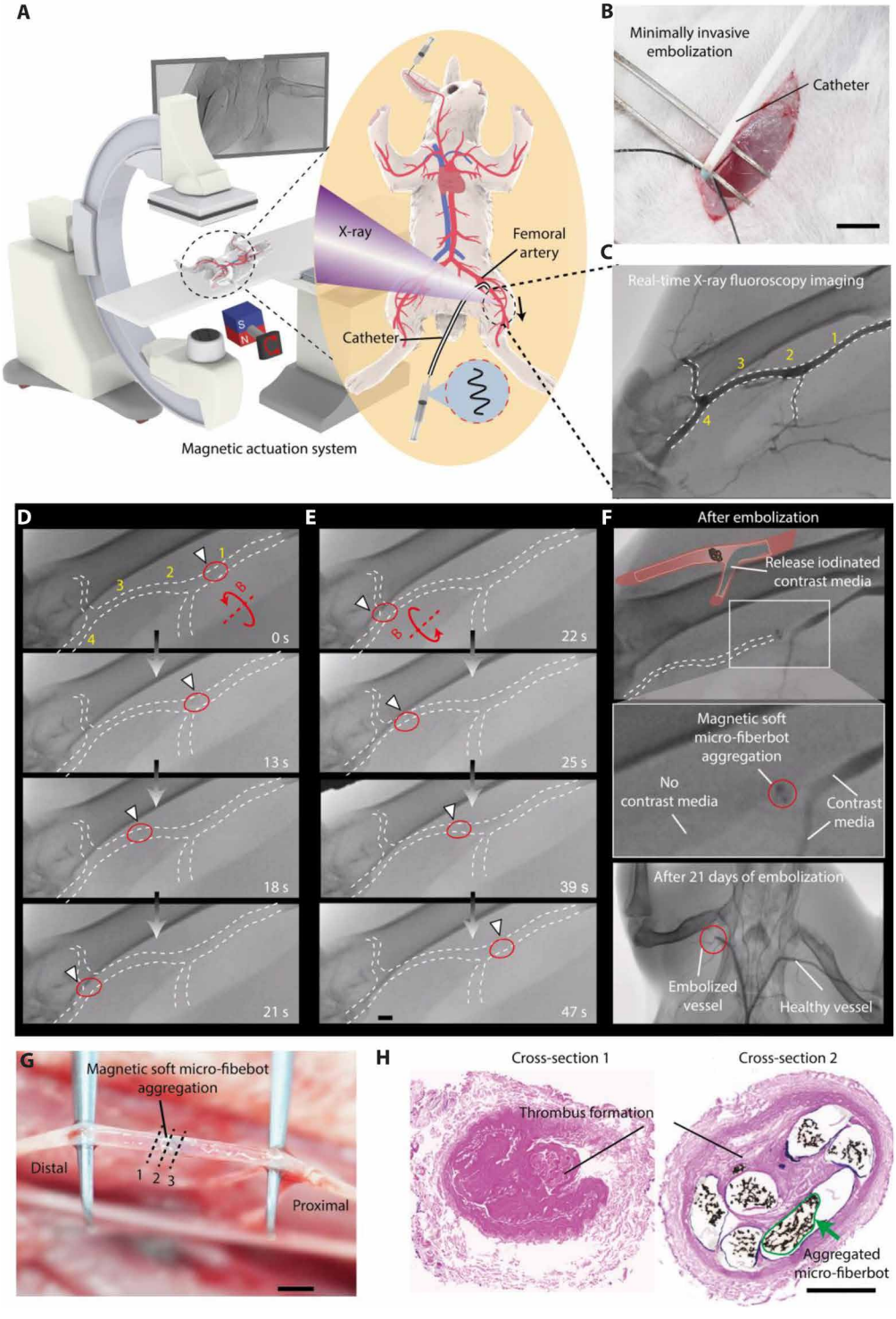

Fig. 7. Robotic embolization in a rabbit blood vessel in vivo. (**A**) Schematic illustration of robotic embolization in rabbit blood vessel on the leg under real-time fluoroscopy. (**B**) The magnetic soft microfiberbot is released into the blood vessel by a catheter. Scale bar, 5 mm. (**C**) The angiology of targeted blood vessel before embolization by infusing iodinated contrast media. (**D**) Fluoroscopy images of microfiberbot navigating from site 1 to site 4. (**E**) Fluoroscopy images of microfiberbot returning from site 4 to site 2 and aggregated. (**F**) The angiology of blood vessel after embolization by infusing iodinated contrast medium. (**G**) The blood vessel is separated for histological analysis 3 weeks after embolization. Scale bar in (D) to (G), 1 mm. (**H**) The H&E staining cross-sectional images of the blood vessel. Cross sections 1 and 2 show the formation of thrombus after embolization. Scale bar, 250 μm.

(Fig. 7C). Guided by fluoroscopic imaging (x-ray), the microfiberbot is helically propelled from site 1 to site 4 (Fig. 7D), returned to site 2, and eventually aggregated at site 2 (Fig. 7E and movie S14). To validate the completed embolization, we then obtained the angiography of the femoral artery by injecting iodinated contrast medium (Fig. 7F). Before embolization, we can see iodinated contrast medium throughout the femoral artery, suggesting a normal flow in the artery. After embolization, no contrast medium was observed because of the blockage of the flow by the aggregated microfiberbot. The angiography conducted 3 weeks after embolization indicated that the microfiberbots have successfully facilitated a stable vascular embolism, with no signs of recanalization. The presence of the aggregated microfiberbot blocked the blood flow from the proximal to the distal end of the vessel, which led to the formation of thrombosis inside the artery, as validated by the histological analysis 3 weeks after embolization (Fig. 7, G and H). It is worth noting that no inflammation or pathological abnormalities were observed from the hematoxylin and eosin (H&E) staining results of the main organs, including the lung, liver, spleen, kidney, and heart, after 3 weeks (fig. S13). Additionally, compared with those of an untreated control group, the numbers of blood cells, such as red blood cells (RBCs), white blood cells, platelets, and lymphocytes, after the robotic embolization procedure remained at normal levels after 3 weeks (fig. S14), suggesting that the proposed robotic embolization by magnetically steering microfiberbots was safe.

DISCUSSION

Conventional embolization surgery by threading passive catheters to the target lesion is largely limited by the low steerability in complex blood vessels (especially in submillimeter regions) and accumulated radiation risk by manual operation. We developed magnetic soft microfiberbots that can perform embolization with high steerability by remotely controlling a

6-DOF robotic arm. With a helical magnetization along its body, the microfiberbot can be magnetically steered via helical propulsion in blood vessels and perform on-demand aggregation at the target lesion to occlude the blood flow. Using demonstrations in submillimeter neurovascular vessel phantoms and in vivo rabbit femoral artery, we validated the potential for performing robotic embolization.

Our microfiberbots are still in their infancy, and we provide the following considerations for their clinical translation in the future. First, we have only demonstrated a microfiberbot with $D = 800$ μm for embolization in submillimeter blood vessels in this work. Actually, the helical diameter D of the microfiberbot can be effectively tuned by changing the geometry of the cylinder mold (Fig. 1B). If large aneurysms or blood vessels are encountered, microfiberbots with larger diameters may be selected. Also, we have shown that two aggregated microfiberbots can enhance the blocking rate (Fig. 6); thus, multiple microfiberbots can be deployed to the target lesion, if needed.

Second, although the soft matrix of SEBS has been approved by the US Food and Drug Administration (FDA) for intravascular applications (*41*), the ferromagnetic NdFeB particles may induce safety concerns for long-term implantation. In this regard, we can first coat a protective layer of pure SEBS shell using the thermal drawing technique (Fig. 1) and then dip-coat a thin layer of hydrogel (15 μm) on the whole body of the microfiberbot to enhance biocompatibility and hemocompatibility (fig. S15). This protective layer–coating technique has been widely adopted to reduce the toxicity of NdFeB-embedded composites (*22*, *23*, *33*, *42*–*44*). According to the cell viability test and hemolysis assay, we show that the hydrogel skin can substantially reduce toxicity (cell viability, 96%; fig. S16) and hemolytic effect (hemolysis, 1%; fig. S17). Third, to realize the precise control of microfiberbots in tortuous blood vessels, an advanced positioning system is required. In addition to the fluoroscopy, we show that our microfiberbot can also be tracked using ultrasound imaging. An ex vivo demonstration in a porcine blood vessel is provided to validate the tracking capability under ultrasound imaging (fig. S18). Other approaches, such as photoacoustic computed tomography, may also be helpful in obtaining higher spatiotemporal resolution (*45*).

Last, a faster thrombus formation is always desired for occluding the blood flow, leading to a successful embolization. In this regard, we present two potential solutions that have been reported in the literature for enhancing embolization efficiency. The first solution is to coat the microfiberbot with thrombin (*46*) such that blood cells can be absorbed into the microfiberbot, as validated by the reduced blood clotting index and scanning electron microscope images in fig. S19. The formed thrombus can resist a pressure of up to 22 kPa, which is large enough to block the blood flow in vivo (fig. S20). The second solution is to further coat the microfiberbot with a thin functional layer (20 μm) of iron oxide (Fe_3O_4) nanoparticles that can generate heat upon radio frequency (RF) stimulation (fig. S15). By remotely heating the aggregated microfiberbot at the target lesion via an RF coil (200 kHz), we can generate local hyperthermia that promotes thrombus formation. In vitro demonstration in the blood vessel phantom shows that a thrombus can be formed within 5 min (fig. S21). The mechanism of local hyperthermia–induced thrombus formation lies in the activation and aggregation of platelets. When the temperature increases to about 41°C, platelets are activated in vivo and aggregate to form a thrombus. This mechanism has been reported in the literature (*47*–*50*) and is also validated by our experiments in which the activated coagulation time of the porcine blood decreases as the temperature rises from 37° to 50°C (fig. S22). In summary, we envisage that our magnetic soft microfiberbots will pave the way for the untethered robotic embolization of cerebral aneurysms and brain tumors in the future.

MATERIALS AND METHODS

Fabrication of magnetic soft microfiberbots

Ferromagnetic NdFeB particles with an average diameter of 5 μm were purchased from Guangzhou XND Co. Ltd.; the soft elastomeric matrix SEBS materials (Kraton G1657) were purchased from KRATON Co. Ltd.; the supporting polycarbonate (PC) pellets (Makrolon ET3113) were purchased from Covestro AG Co. Ltd. All materials were used as received. The ferromagnetic NdFeB particles were mixed in a predissolved SEBS/hexane solution (14.3 vol %) with a volume ratio of 1:4 between NdFeB and SEBS. After mechanical stirring for 30 min and ultrasonic dispersing for 1 hour, the NdFeB/SEBS/hexane suspensions were poured and doctor-bladed on polytetrafluoroethylene (PTFE) films and dried in a fume hood for 10 hours. Once fully dried, the resulting NdFeB/SEBS thin films were peeled from PTFE and cut into small slices of magnetic SEBS (M-SEBS). For M-SEBS core fabrication, the yielded M-SEBS slices were loaded in mold between a thermocompressor (Qien, Wuhan Qien Sci. & Tech. Co. Ltd.) and thermally pressed at 180°C into M-SEBS cylinders. For supporting PC cladding fabrication, the fully dried PC pellets were loaded in mold between the thermocompressor and thermally pressed at 230°C into cuboids. The PC cuboids were lathed and drilled into PC tubes with an inner diameter slightly larger than M-SEBS cylinders. The yielded M-SEBS cylinders were inserted into PC tubes for monolithic preforms. The magnetic composites were prepared through the dispersion of unmagnetized magnetic microparticles (NdFeB) in soft elastomeric matrix SEBS through chemical solution. Because of the limited drawing ability of the soft magnetic elastomer composite, we induced thermoplastic PC as sacrificial cladding for codrawing. After thermal consolidation in a LEGO-like way, the preforms consisting of a magnetic soft core and sacrificial cladding were later thermally drawn into magnetic microfibers with different diameters (Fig. 1C) at 230°C in a custom thermal draw tower.

Thermal drawing of magnetic microfibers

The resulting preforms consisted of an M-SEBS core and PC cladding that were thermally drawn into M-SEBS/PC fibers, referred to as magnetic fibers, at 230°C in a custom thermal drawing tower. With a drawing ratio between 100 and 200, the diameter of magnetic fibers can be tuned between 20 and 90 μm. To enhance the functionality of microfiberbot, the functional layer was induced to the soft core preform. The preforms consist of a magnetic soft core (M-SEBS) and a functional layer (fig. S15). The functional layer can be chosen according to different situations. For example, to enhance biocompatibility and hemocompatibility, a pure polymer protect layer can prevent corrosion of ferromagnetic particles (NdFeB). In addition, to enhance the embolization efficiency, a functional layer containing Fe_3O_4 nanoparticles can promote thrombus formation via RF heating.

Mechanical testing

The 80 mm–by–80 mm–by–2 mm M-SEBS thin film was cut into dumbbell test specimens using a standard part cutter. The mechanical testing was subjected to standard test methods (ASTM D412) on a mechanical testing machine at a displacement rate of 5 mm/s (width: 8 mm; gauge length: 60 mm).

Fabrication of magnetic soft microfiberbots

The magnetic microfibers were first magnetized by a 2.5-T impulse magnetic field generated by a digital pulse magnetizer (Beijing Eusci Technology Ltd). The fibers with PC cladding were then wrapped with identity helical parameters on a high–thermal conductivity rod by tweezers. Adhesive tape was applied to ensure that the fiber tightly contacted the rod. The rod with microfibers was then placed on a hot plate at 90°C for 30 min. After the magnetic microfiber was molded into a helical-shaped structure, the robots were detached from the rods. Sacrificial PC cladding was chemically selectively removed by *N*,*N*-dimethylacetamide (Sinopharm Chemical Reagent Co. Ltd.) until the cladding was completely dissolved. Finally, the robot was cut into the desired structure parameters.

In vitro experiments

To demonstrate the catheter-assisted deployment and steerability of microfiberbots in submillimeter regions, as presented in Figs. 3, C and D, and 4 with movies S5 and S6, vessel phantoms coated with hydrogel were used to mimic the mechanical properties of real vessels (see fig. S10). These silicone vessel models were filled with blood analog. To assess the repeatability of the navigational task, each experiment was conducted three times. In the demonstration of in vitro aneurysm embolization presented in Fig. 5, A and B, with movie S10, the iodinated contrast medium was released to evaluate embolization under fluoroscopic guidance (DSA, CGO-2100, Wandong). In the demonstration of in vitro embolization particle protection presented in Fig. 5, E to H, with movie S12, polystyrene microspheres with an average diameter of 250 μm (Yuan biotech) were used.

Ex vivo experiments under real-time ultrasound imaging

The medical imaging system compatibility of the magnetic soft microfiberbot was demonstrated in a porcine coronary artery ex vivo under real-time ultrasound imaging. The porcine hearts were obtained from Shenzhen Advanced Medical Services Co. Ltd. A solution of glycerol (Sigma-Aldrich) in deionized (DI) water was used as a blood analog (viscosity was around 4 mPa·s), and the arteries were connected to a programmable pump (Longer Pump) to create the bloodstream (100 mm/s). The wireless portable ultrasound probe (SonoStar) with a maximum frequency of 14 MHz was used for real-time guidance of the magnetic soft microfiberbot. After injection into the artery, the magnetic soft microfiberbot was magnetically actuated to swim with the flow to the targeted site. When the magnetic field was removed, the magnetic soft microfiberbot was anchored to the target blood vessel wall while withstanding the flow. The ultrasound imaging in pulse repetition frequency mode verified the anchoring of the robot in dynamic flow. The magnetic soft microfiberbot was also magnetically actuated to swim against the flow and was retrieved by a catheter inside the artery vessels.

Hydrogel skin fabrication

The dip-coating methods were used to create a hydrogel layer on the magnetic soft microfiberbot. The monomer of the hydrogel layer was acrylamide (AAm) (Sigma-Aldrich, A8887). The silane coupling agent was 3-(trimethoxysilyl) propyl methacrylate (TMSPMA). The chain transfer agent (CTA) was (3-mercaptopropyl) trimethoxysilane (Sigma-Aldrich, 175617). For a 1-ml solution of AAm (2 M of DI water), 1 μl of CTA (10% volume ratio in tetrahydrofuran), 10 μl of acetic acid (0.1 M of DI water), and 5.7 μl of TMSPMA were added, followed by vortex mixing for 60 s, and then 50 mg of thrombin (2000 U/mg, Shanghai Yuanye Bio-Technology Co. Ltd.) was added. The bare magnetic fiber was treated with plasma within 60 s to form the network of hydrophilic groups. The treated magnetic fiber was fixed to a homemade machine and immersed in the pre-gel solution (fig. S19). Last, the hydrogel-coated microfiber was sealed in a bottle with saturated humidity and stored in an oven at room temperature for 24 hours.

Cell toxicity assay

A human cardiac microvascular endothelial cell line was cultured and removed from the flask using enzymatic digestion (trypsin/EDTA). The cell suspension was centrifuged at 1000 rpm for 5 min. The cell suspension was resuspended in medium to adjust the density to 1×10^5 cells/ml. A multichannel pipette was used to add 100 μl of medium to the peripheral wells of a 96-well tissue culture micro titer plate and to add 100 μl of cell suspension at a density of 1×10^5 cells/ml to the remaining wells. Cells were incubated for 24 hours (5% CO_2 at 37°C, >90% humidity) for exponential growth. The medium was aspirated after 24 hours of incubation. To evaluate the cell toxicity of M-SEBS composites, 100 μl of the 100% of sample leaching solution including negative control, positive control, bare magnetic fiber, and hydrogel-coated magnetic fiber was added for treatment. Cells were incubated for another 48 hours (5% CO_2 at 37°C, >90% humidity). After removing the cocultured material and replacing the medium, 10 μl of CCK-8 solution (AR1199, Boster, China) was added to each well, and the plate was placed on a microtiter plate photometer (Multiskan FC, Thermo Fisher Scientific) equipped with a 450-nm filter to measure the absorbance. The cell viability was calculated according to the following equation:

$$\text{Cell viability}(\%) = \frac{C_{\text{sample}} - C_{\text{blank}}}{C_{\text{control}} - C_{\text{blank}}} \times 100\% \quad (3)$$

where C_{sample} is the absorbance of sample, C_{control} is the absorbance of control (without sample), and C_{blank} is the absorbance of blank group.

Live/dead assay

Human cardiac microvascular endothelial cell line was cultured and removed from the flask using enzymatic digestion (trypsin/EDTA). The cell suspension was centrifuged at 1000 rpm for 5 min. A total of 5×10^5 cells was inoculated in each well of a six-well plate and incubated in a CO_2 incubator (5% CO_2 at 37°C, >90% humidity) for 24 hours to allow the cells to adhere to the well. Subsequently, the medium was removed, 2 ml of the sample leaching solution from each group was added to the six-well plate, and incubation was continued for 48 hours. After cells were washed twice with phosphate-buffered saline (PBS) buffer, 0.5 ml of staining solution (KTA1001, Abbkine, China) was added to each well and incubated for 15 min at 37°C protected from light. After being washed two more times with PBS, the cells were placed under a fluorescent microscope and photographed.

Hemolysis rate assay

Newly collected immune blood (20 ml; Shenzhen Advanced Medical Services Co. Ltd.) was added with 1 ml of potassium oxalate (20 g/liter) to prepare fresh anticoagulated immune blood. Fresh anticoagulated rabbit blood (8 ml) was taken and diluted with 10 ml of normal saline. Three samples of 5 g each were weighted. After being rinsed with tap water, the samples were rinsed with distilled water, with the water absorbed with filter paper and put in a test tube, and 10 ml of normal saline was added to each tube; for the negative

control, 10 ml of normal saline of the same batch number was added to each tube; for the positive control, 10 ml of distilled water was added to each tube. To evaluate the hemolysis rate of M-SEBS composites, 0.2 ml of diluted rabbit blood was added to either bare magnetic fiber or hydrogel-coated magnetic fiber for treatment, placed in a 37°C water bath, and continued to incubate for 60 min. The liquid in each tube was poured out and centrifuged for 5 min (2500 rotations/min), and the absorbance was measured with a spectrophotometer at a wavelength of 545 nm. The hemolysis rate was calculated according to the following equation:

$$\text{Hemolysis rate}\ (\%) = \frac{H_{\text{sample}} - H_{\text{neg}}}{H_{\text{pos}}} \times 100\% \quad (4)$$

where H_{sample} is the absorbance at 545 nm of the sample, H_{neg} is the absorbance of negative group, and H_{pos} is the absorbance of positive group.

Blood clotting index test

First, the microfiberbot with 10 mg of pure hydrogel coating and thrombin hydrogel coating was placed into the polypropylene dish and prewarmed at 37°C for 5 min. Second, 4.5 ml of fresh anti-coagulated porcine blood was added with 0.5 ml of 0.1 M solution of calcium chloride to prepare fresh blood samples. Third, 100 μl of the blood was immediately coated onto the materials for 10 s. Then, 10 ml of DI water was added to the dish and shaken at 50 rpm for 10 min to lyse RBCs that were not stuck in the clot. The absorbance of the resulting hemoglobin solution (sample) was measured at 540 nm by a Multiskan microplate reader (Multiskan GO, Thermo Fisher Scientific), and absorbance of 100 μl of clotted whole blood in 10 ml of DI water was used as the control. Finally, the blood clotting index of different materials was calculated using the following equation:

$$\text{Blood clotting index}(\%) = \frac{S_{\text{sample}}}{S_{\text{control}}} \times 100\% \quad (5)$$

Preparation of RBC solution

A volume of 5 ml of fresh anti-coagulated porcine blood was taken into a blood centrifuge tube. RBCs were centrifuged at 200*g* for 20 min at room temperature, and the supernatant was gently removed. RBCs were washed three times with 500 μl of 1× PBS solution and finally resuspended with 500 μl of 1× PBS.

In vivo animal experiment setup

The 8- to 10-week-old male New Zealand rabbits, weighing 1.5 to 2.0 kg, were obtained from Shenzhen Advanced Medical Services Co. Ltd. Ethical approval from the Institutional Animal Care and Use Committee was obtained before the research (AMS C2305004 R). The rabbit was anesthetized before the embolization procedure. The femoral artery was exposed through a small incision, and then the femoral artery was accessed using a standard 22-gauge needle and a 4-Fr sheath (Glidesheath, Terumo). Under fluoroscopic guidance (DSA, CGO-2100, Wandong), the iodinated contrast medium was released to obtain the blood vessel frame, and the magnetic soft microfiberbot was gently injected into the artery through a 2.6-Fr catheter (Headway 27 microcatheter, Terumo). The rotating magnetic field was generated by a cubic NdFeB magnet (50 mm in diameter and 50 mm in height). The magnetic soft microfiberbots were reliably steered and navigated by helical propulsion in the blood vessel. After the robot contracted into an aggregation state, the magnetic field was removed, and iodinated contrast medium was gently released to obtain the angiography (see Fig. 7). Then, the catheter and sheath were removed, and the wound was sutured. After 3 weeks of post-surgery, tissue sections in embolization regions were prepared and stained with H&E for histological examinations.

Analysis and simulation

Magnetic fields around a cubic magnet were calculated using the commercial software COMSOL Multiphysics 6.0. Finite element simulations of shape morphing of microfiberbot were conducted using the commercial software ABAQUS/Standard 2017. The NdFeB embedded magnetic composite was modeled as the ideal hard-magnetic soft material with a shear modulus of 1 MPa and a residual magnetization $\mathbf{M} = 120$ kA/m. To account for the interaction between magnetic composite with embedded NdFeB particles and the external magnetic field $\mathbf{B}$, we adopted a user element (UEL) subroutine based on the continuum framework (*51*, *52*). The magnetic torque density $\boldsymbol{\tau}$ can be implemented by computing the magnetic Cauchy stress $\boldsymbol{\sigma}^{\text{magnetic}} = -\mathbf{B}\otimes\mathbf{FM}$, where $\mathbf{F}$ is the deformation gradient and operator $\otimes$ represents a dyadic product that takes two vectors to yield a second-order tensor. The blood vessel is simplified as a rigid tube. The contact between the microfiberbot and the blood vessel is modeled as "hard contact, No penetration" with a friction coefficient of 0.1. The maximum contact pressure was directly extracted from simulation results (see fig. S2B). All simulations were checked with convergence.

Statistical tests

Experimental values were obtained by conducting measurements N times, with subsequent statistical analysis carried out using specialized data statistics software. For experiments involving a single measurement ($N = 1$), only the raw measurement values were reported. When experiments were repeated N times, the results were presented in the figures as means ± SD.

Supplementary Materials

This PDF file includes:

Text
Figs. S1 to S22
Table S1
References (*53-56*)

Other Supplementary Material for this manuscript includes the following:

Movies S1 to S14
MDAR Reproducibility Checklist

REFERENCES AND NOTES

1. Y. Fan, X. Zhang, C. Gao, S. Jiang, H. Wu, Z. Liu, T. Dou, Burden and trends of brain and central nervous system cancer from 1990 to 2019 at the global, regional, and country levels. *Arch. Public Health* **80**, 209 (2022).
2. A. Burlakoti, J. Kumaratilake, J. Taylor, M. Henneberg, Relationship between cerebral aneurysms and variations in cerebral basal arterial network: A morphometric cross-sectional study in Computed Tomography Angiograms from a neurointerventional unit. *BMJ Open* **11**, e051028 (2021).
3. G. Toth, R. Cerejo, Intracranial aneurysms: Review of current science and management. *Vasc. Med.* **23**, 276–288 (2018).
4. J. J. Leyon, T. Littlehales, B. Rangarajan, E. T. Hoey, A. Ganeshan, Endovascular embolization: Review of currently available embolization agents. *Curr. Probl. Diagn. Radiol.* **43**, 35–53 (2014).
5. B. S. Peters, P. R. Armijo, C. Krause, S. A. Choudhury, D. Oleynikov, Review of emerging surgical robotic technology. *Surg. Endosc.* **32**, 1636–1655 (2018).

6. Y. Fu, H. Liu, W. Huang, S. Wang, Z. Liang, Steerable catheters in minimally invasive vascular surgery. *Int. J. Med. Robot.* **5**, 381–391 (2009).
7. S. Gunduz, H. Albadawi, R. Oklu, Robotic devices for minimally invasive endovascular interventions: A new dawn for interventional radiology. *Adv. Intell. Syst.* **3**, 2000181 (2021).
8. J. Gould, Breaking down the epidemiology of brain cancer. *Nature* **561**, S40–S41 (2018).
9. R. Huang, J. Boltze, S. Li, Strategies for improved intra-arterial treatments targeting brain tumors: A systematic review. *Front. Oncol.* **10**, 1443 (2020).
10. A. I. Qureshi, V. Janardhan, R. A. Hanel, G. Lanzino, Comparison of endovascular and surgical treatments for intracranial aneurysms: An evidence-based review. *Lancet Neurol.* **6**, 816–825 (2007).
11. S. Juvela, K. Poussa, H. Lehto, M. Porras, Natural history of unruptured intracranial Aneurysms. *Stroke* **44**, 2414–2421 (2013).
12. G. Guglielmi, F. Viñuela, G. Duckwiler, J. Dion, P. Lylyk, A. Berenstein, C. Strother, V. Graves, V. Halbach, D. Nichols, N. Hopkins, R. Ferguson, I. Sepetka, Endovascular treatment of posterior circulation aneurysms by electrothrombosis using electrically detachable coils. *J. Neurosurg.* **77**, 515–524 (1992).
13. S. Vaidya, K. R. Tozer, J. C. Chen, An overview of embolic agents. *Semin. Intervent. Radiol.* **25**, 204–215 (2008).
14. J. Hu, H. Albadawi, B. W. Chong, A. R. Deipolyi, A. Sheth, A. Khademhosseini, R. Oklu, Advances in biomaterials and technologies for vascular embolization. *Adv. Mater.* **31**, e1901071 (2019).
15. C. Y. Wang, J. Hu, R. A. Sheth, R. Oklu, Emerging embolic agents in endovascular embolization: An overview. *Prog. Biomed. Eng. (Bristol)* **2**, 012003 (2020).
16. B. J. Nelson, S. Gervasoni, P. W. Chiu, L. Zhang, A. Zemmar, Magnetically actuated medical robots: An in vivo perspective. *Proc. IEEE* **110**, 1028–1037 (2022).
17. H. Tillander, Magnetic guidance of a catheter with articulated steel tip. *Acta Radiol.* **35**, 62–64 (1951).
18. N. Gudino, J. A. Heilman, J. J. Derakhshan, J. L. Sunshine, J. L. Duerk, M. A. Griswold, Control of intravascular catheters using an array of active steering coils. *Med. Phys.* **38**, 4215–4224 (2011).
19. T. Gopesh, J. H. Wen, D. Santiago-Dieppa, B. Yan, J. S. Pannell, A. Khalessi, A. Norbash, J. Friend, Soft robotic steerable microcatheter for the endovascular treatment of cerebral disorders. *Sci. Robot.* **6**, eabf0601 (2021).
20. M. F. Phelan, M. E. Tiryaki, J. Lazovic, H. Gilbert, M. Sitti, Heat-mitigated design and Lorentz force-based steering of an MRI-driven microcatheter toward minimally invasive surgery. *Adv. Sci.* **9**, 2105352 (2022).
21. L. Wang, D. Zheng, P. Harker, A. B. Patel, C. F. Guo, X. Zhao, Evolutionary design of magnetic soft continuum robots. *Proc. Natl. Acad. Sci. U.S.A.* **118**, e2021922118 (2021).
22. Y. Kim, G. A. Parada, S. Liu, X. Zhao, Ferromagnetic soft continuum robots. *Sci. Robot.* **4**, eaax7329 (2019).
23. Y. Kim, E. Genevriere, P. Harker, J. Choe, M. Balicki, R. W. Regenhardt, J. E. Dmytriw, A. B. Patel, X. Zhao, Telerobotic neurovascular interventions with magnetic manipulation. *Sci. Robot.* **7**, eabg9907 (2022).
24. A. Azizi, C. C. Tremblay, K. Gagné, S. Martel, Using the fringe field of a clinical MRI scanner enables robotic navigation of tethered instruments in deeper vascular regions. *Sci. Robot.* **4**, eaax7342 (2019).
25. L. Pancaldi, P. Dirix, A. Fanelli, A. M. Lima, N. Stergiopulos, P. J. Mosimann, D. Ghezzi, M. S. Sakar, Flow driven robotic navigation of microengineered endovascular probes. *Nat. Commun.* **11**, 6356 (2020).
26. C. Chautems, A. Tonazzini, Q. Boehler, S. H. Jeong, D. Floreano, B. J. Nelson, Magnetic continuum device with variable stiffness for minimally invasive surgery. *Adv. Intell. Syst.* **2**, 1900086 (2019).
27. J. Hwang, J. Kim, H. Choi, A review of magnetic actuation systems and magnetically actuated guidewire- and catheter-based microrobots for vascular interventions. *Intell. Serv. Robot.* **13**, 1–14 (2020).
28. J. Law, X. Wang, M. Luo, L. Xin, X. Du, W. Dou, T. Wang, G. Shan, Y. Wang, P. Song, X. Huang, J. Yu, Y. Sun, Microrobotic swarms for selective embolization. *Sci. Adv.* **8**, eabm5752 (2022).
29. N. Li, F. Michaud, Z. Nosrati, D. Loghin, C. Tremblay, R. Plantefève, K. Saatchi, U. O. Häfeli, S. Martel, G. Soulez, MRI-compatible injection system for magnetic microparticle embolization. *IEEE Trans. Biomed. Eng.* **66**, 2331–2340 (2018).
30. Z. Li, Z. Chen, Y. Gao, Y. Xing, Y. Zhou, Y. Luo, W. Xu, Z. Chen, X. Gao, K. Gupta, K. Anbalakan, L. Chen, C. Liu, J. Kong, H. L. Leo, C. Hu, H. Yu, Q. Guo, Shape memory micro-anchors with magnetic guidance for precision micro-vascular deployment. *Biomaterials* **283**, 121426 (2022).
31. J. I. Bilbao, A. Martínez-Cuesta, F. Urtasun, O. Cosín, Complications of embolization. *Semin. Intervent. Radiol.* **23**, 126–142 (2006).
32. Z. Ren, R. Zhang, R. H. Soon, Z. Liu, W. Hu, P. R. Onck, M. Sitti, Soft-bodied adaptive multimodal locomotion strategies in fluid-filled confined spaces. *Sci. Adv.* **7**, eabh2022 (2021).
33. T. Wang, H. Ugurlu, Y. Yan, M. Li, M. Li, A. M. Wild, E. Yildiz, M. Schneider, D. Sheehan, W. Hu, M. Sitti, Adaptive wireless millirobotic locomotion into distal vasculature. *Nat. Commun.* **13**, 4465 (2022).
34. D. Gonzalez-Rodriguez, L. Guillou, F. Cornat, J. Lafaurie-Janvore, A. Babataheri, E. de Langre, A. I. Barakat, J. Husson, Mechanical criterion for the rupture of a cell membrane under compression. *Biophys. J.* **111**, 2711–2721 (2016).
35. E. A. G. Peeters, C. W. J. Oomens, C. V. C. Bouten, D. L. Bader, F. P. T. Baaijens, Mechanical and failure properties of single attached cells under compression. *J. Biomech.* **38**, 1685–1693 (2005).
36. A. W. Mahoney, J. J. Abbott, Generating rotating magnetic fields with a single permanent magnet for propulsion of untethered magnetic devices in a lumen. *IEEE Trans. Robot.* **30**, 411–420 (2013).
37. J. J. Abbott, E. Diller, A. J. Petruska, Magnetic methods in robotics. *Annu. Rev. Control Robot. Auton. Syst.* **3**, 57–90 (2020).
38. B. Wang, K. F. Chan, K. Yuan, Q. Wang, X. Xia, L. Yang, H. Ko, Y.-X. J. Wang, J. J. Y. Sung, P. W. Y. Chiu, L. Zhang, Endoscopy-assisted magnetic navigation of biohybrid soft microrobots with rapid endoluminal delivery and imaging. *Sci. Robot.* **6**, eabd2813 (2021).
39. Q. Wang, X. Du, D. Jin, L. Zhang, Real-time ultrasound doppler tracking and autonomous navigation of a miniature helical robot for accelerating thrombolysis in dynamic blood flow. *ACS Nano* **16**, 604–616 (2022).
40. L. Zarrinkoob, K. Ambarki, A. Wåhlin, R. Birgander, A. Eklund, J. Malm, Blood flow distribution in cerebral arteries. *J. Cereb. Blood Flow Metab.* **35**, 648–654 (2015).
41. U.S. Food and Drug Administration (FDA), *Class 2 Medical Device: Swan-Ganz Catheters* (510(K) Number: K193466, FDA, 2020).
42. W. Hu, G. Z. Lum, M. Mastrangeli, M. Sitti, Small-scale soft-bodied robot with multimodal locomotion. *Nature* **554**, 81–85 (2018).
43. C. Zhou, Y. Yang, J. Wang, Q. Wu, Z. Gu, Y. Zhou, X. Liu, Y. Yang, H. Tang, Q. Ling, L. Wang, J. Zang, Ferromagnetic soft catheter robots for minimally invasive bioprinting. *Nat. Commun.* **12**, 5072 (2021).
44. Y. Yang, J. Wang, L. Wang, Q. Wu, L. Ling, Y. Yang, S. Ning, Y. Xie, Q. Cao, L. Li, J. Liu, Q. Ling, J. Zang, Magnetic soft robotic bladder for assisted urination. *Sci. Adv.* **8**, q1456 (2022).
45. Z. Wu, L. Li, Y. Yang, P. Hu, Y. Li, S. Y. Yang, L. V. Wang, W. Gao, A microrobotic system guided by photoacoustic computed tomography for targeted navigation in intestines in vivo. *Sci. Robot.* **4**, eaax0613 (2019).
46. D. A. Nicholson, J. F. Cockburn, A. E. Bradshaw, P. Dawson, Thrombin-soaked embolization coils: The effect on whole blood clotting time. *Clin. Radiol.* **46**, 108–110 (1992).
47. G. Lippi, M. Franchini, G. Targher, Arterial thrombus formation in cardiovascular disease. *Nat. Rev. Cardiol.* **8**, 502–512 (2011).
48. S. V. Strother, J. M. Bull, S. A. Branham, Activation of coagulation during therapeutic whole body hyperthermia. *Thromb. Res.* **43**, 353–360 (1986).
49. T. Iba, J. Helms, M. Levi, J. H. Levy, The role of platelets in heat-related illness and heat-induced coagulopathy. *Thromb. Res.* **231**, 152–158 (2023).
50. O. Suzuki, S. Miyachi, T. Okamoto, A. Ito, M. Shinkai, H. Honda, T. Kobayashi, M. Negoro, J. Yoshida, Local hyperthermia enhances thrombosis in aneurysms containing platinum coils. *Interv. Neuroradiol.* **10**, 203–211 (2004).
51. L. Wang, Y. Kim, C. F. Guo, X. Zhao, Hard-magnetic elastica. *J. Mech. Phys. Solids* **142**, 104045 (2020).
52. R. Zhao, Y. Kim, S. A. Chester, P. Sharma, X. Zhao, Mechanics of hard-magnetic soft materials. *J. Mech. Phys. Solids* **124**, 244–263 (2019).
53. Y. Alapan, U. Bozuyuk, P. Erkoc, A. C. Karacakol, M. Sitti, Multifunctional surface microrollers for targeted cargo delivery in physiological blood flow. *Sci. Robot.* **5**, eaba5726 (2020).
54. Q. Wang, K. F. Chan, K. Schweizer, X. Du, D. Jin, S. C. H. Yu, B. J. Nelson, L. Zhang, Ultrasound Doppler-guided real-time navigation of a magnetic microswarm for active endovascular delivery. *Sci. Adv.* **7**, eabe5914 (2021).
55. F. E. Stokes, R. A. King, *Flow-Induced Vibration of Helical Coil Compression Springs* (North-Holland, 1983).
56. G. Parada, Y. Yu, W. Riley, S. Lojovich, D. Tshikudi, Q. Ling, Y. Zhang, J. Wang, L. Ling, Y. Yang, S. Nadkarni, C. Nabzdyk, X. Zhao, Ultrathin and robust hydrogel coatings on cardiovascular medical devices to mitigate thromboembolic and infectious complications. *Adv. Healthc. Mater.* **9**, e2001116 (2020).

Acknowledgments

Funding: This work was supported by the National Natural Science Foundation of China (52188102, 51820105008, 51572096, 2022YFC2408100, 11272369, and 62175082) and Huazhong University of Science and Technology Interdisciplinary Research Support Program (2023JCYJ044 and 2023JCYJ039). **Author contributions:** J.Z., G.T., G.-Z.Y., and X.L. conceived the idea and designed the research. X.L. and Y.X. performed the thermal drawing experiments. X.L. and F.L. constructed the experimental platform. X.L., F.L., and N.L. performed other experiments and analyzed the data. L.W. and X.L. performed the theoretical analysis and numerical calculations. X.L., L.W., Y.X., G.-Z.Y., G.T., and J.Z. wrote the manuscript with input from all authors. All authors participated in drafting the manuscript and discussing and interpreting the data. **Competing interests:** J.Z. and X.L. have a provisional patent application on the fundamental principles and designs of transforming untethered magnetic soft microfiberbot for endovascular intervention. The other authors declare that they have no competing financial interests. **Data and materials availability:** All data are available in the main text or the Supplementary Materials and are available online at http://doi.org/10.5281/zenodo.7994833.

Submitted 19 February 2023
Accepted 24 January 2024
Published 21 February 2024
10.1126/scirobotics.adh2479

Science Robotics

Magnetic soft microfiberbots for robotic embolization

Xurui Liu, Liu Wang, Yuanzhuo Xiang, Fan Liao, Na Li, Jiyu Li, Jiaxin Wang, Qingyang Wu, Cheng Zhou, Youzhou Yang, Yuanshi Kou, Yueying Yang, Hanchuan Tang, Ning Zhou, Chidan Wan, Zhouping Yin, Guang-Zhong Yang, Guangming Tao, and Jianfeng Zang

Sci. Robot. **9** (87), eadh2479. DOI: 10.1126/scirobotics.adh2479

Editor's summary

As a minimally invasive treatment for aneurysms and brain tumors, surgeons typically insert a slender catheter through the femoral artery and guide it through blood vessels to deliver embolic agents. However, this method of embolization can be difficult to steer through complex vascular networks. A magnetic, soft microfiberbot was developed by Liu*et al.* to perform remotely controlled robotic embolization. The microfiberbot, composed of a magnetized fiber coiled into a helix shape, can conform to different vessel sizes and performs a corkscrew propulsion when subjected to an external magnetic field. The microfiberbots were used to successfully perform in vitro embolization of aneurysm and tumor in phantom blood vessels and in vivo embolization in a rabbit femoral artery. These proposed robots provide a controllable alternative to conventional catheter-based embolization. —Melisa Yashinski

Science Robotics (ISSN 2470-9476) is published by the American Association for the Advancement of Science. 1200 New York Avenue NW, Washington, DC 20005. The title *Science Robotics* is a registered trademark of AAAS.